

AN ATOMS-TO-MESOSCALE APPROACH TO ICE-VAPOR SURFACE DYNAMICS WITH A QUASI-LIQUID INTERFACE

Steven Neshyba^{1,2}, Tia Böttger¹, Rohan Crossland¹, Spencer Racca-Gwozdzik¹, Ella Slattery¹,
Maximilian Bloom¹, Noah Zimmer¹, Ezra Thill¹, Penny Rowe², and Jacob Price¹

¹University of Puget Sound, Tacoma, WA

²NorthWest Research Associates, Redmond, WA

Abstract. We explore the hypothesis that a key factor in determining the dynamics and morphology of faceted ice-vapor surfaces is the quasi-liquid layer that forms at this interface at temperatures above 240 K. We do so by modeling the ice surface as a pair of reaction-diffusion equations in which the time scales of quasi-liquid freezing and melting, horizontal diffusion, and exchanges with the vapor phase are made explicit. Model parameterizations integrated with vapor field around growing and ablating ice crystals. Our results support a differential diffusive slowdown mechanism that compensates for inhomogeneities in the concentration of vapor pressure at the ice-vapor interface, which manifests as a limit cycle in the thickness of the quasiliquid layer and a constant rate of growth or decay of the overall crystal.

Key words. ice, surface, PDE

MSC codes. 35K57, 37M05, 70K05

1. Introduction. Ice crystals that make up cirrus clouds modulate Earth’s climate by reflecting or scattering sunlight before it reaches Earth’s surface, but the extent to which they do that depends on the morphology of those crystals. Although hexagonal prisms dominate, there is a great deal of variation: long and thin hexagonal needles, short and wide plates, indentations and hollowing, and even dendritic forms, like snowflakes. Moreover, facets can be rough on a scale that matters to light of comparable wavelength [1]. Because of this variability, integrating morphologies into climate models remains a formidable task, and contributes to the large uncertainties in climate change prediction.

All this points to a need for better models of ice surface morphology and dynamics. Numerous approaches have been developed, of which Harrington and Pokrifka [2] provide an excellent review. Molecular Dynamics studies have contributed greatly to this effort (see, e.g., reference [3])). Here we focus on two approaches, Classical Nucleation Theory and Continuum theory, because they are particularly relevant to the work presented here.

Classical Nucleation Theory. CNT’s atomistic view of the process of crystal growth goes along the following lines: when a gas-phase molecule (e.g., a water molecule) encounters a crystalline surface, it initially becomes attached to that surface as an “admolecule.” Not yet part of the crystal’s lattice, this admolecule diffuses across the surface until it meets one of two fates: either it fills an unoccupied position in the crystal lattice, or else it returns to the gas phase. New layer formation is governed by a 2D nucleation process in which the step free energy plays a central role [4].

CNT has long framed how we think about ice crystal growth from the vapor phase, but it suffers from two drawbacks. First, it offers little guidance when it comes to describing the behavior of crystals placed in a vapor field that is inhomogeneous on a mesoscopic scale. To be specific, when a growing faceted ice crystal is situated in a supersaturated vapor field, the expectation is that the surrounding water vapor concentration will be drawn down in such a way that parts of the crystal that protrude

out more into the surrounding vapor (i.e., crystal corners) will experience persistently higher vapor pressures than facet centers. CNT predicts that this would result in faster growth at those corners, leading ultimately to dendritic forms (e.g., snowflakes). However, under typical cirrus cloud conditions, it is known that hexagonal prisms resist that tendency, despite those inhomogeneities. Classical nucleation theory has no satisfactory explanation for the persistence of hexagonal prismatic habit in the presence of inhomogeneities in the overlying vapor. (However, see Jayaprakash et al [5]).

A second shortcoming of CNT concerns the presence of a quasi-liquid layer on the surface. This is particular to ice: when the temperature of ice rises above 240 K, both experiment and theoretical studies have shown that the ice/air interface is covered by a quasi-liquid layer (QLL); molecular dynamics studies have shown that water molecules striking the surface are thermalized by the QLL efficiently and quickly (on a picosecond time scale) [6]. The presence of a QLL does not preclude crystalline layering: recent experimental work has shown that steps and ledges may form underneath the QLL, i.e., at the interface between the QLL and the underlying ice [7]. It is clear that CNT is ill-equipped to describe such structures.

1.1. Continuum approaches. A quasi-liquid-continuum model, here referred to as QLC-1, was presented by some of the authors in Neshyba et al [8], henceforth N2016) as a way to address these shortcomings. The relevant state variables are N_{tot} and N_{QLL} , representing the total thickness of the ice surface, and its quasi-liquid part, respectively (see Fig. 1). QLC-1 models the time evolution of these variables using a pair of reaction-diffusion equations, taking into account exchange of QLL molecules with the vapor phase (deposition and ablation), diffusion of QLL molecules across the ice surface, and conversion of QLL molecules to/from the underlying ice.

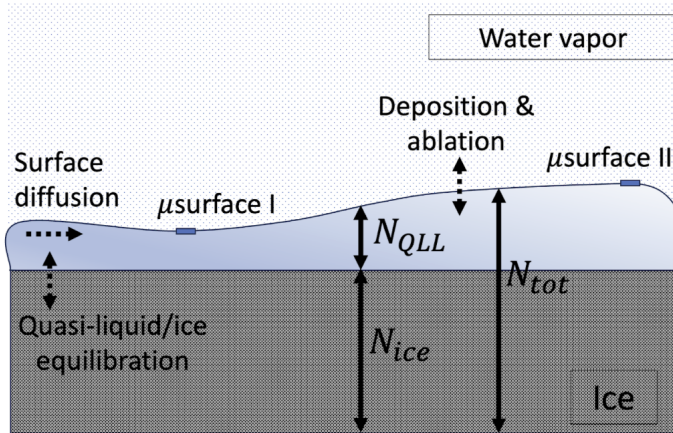


FIG. 1. Visual representation of mesoscale variables N_{tot} , N_{ice} , and N_{QLL} , and processes affecting them, in the QLC-1 and QLC-2 models.

The main insight afforded by QLC-1 is the following: through the interplay of quasiliquid volatility and thickness, an ice surface evolves spontaneously in a way that inhomogeneities in the rate of deposition from the vapor are compensated for by changes in the surface. In other words, QLC-1 provides a mechanism for faceted crystal growth in the presence of an inhomogeneous vapor field, and this faceted growth is mediated by the QLL. N2016 provides a quantitative description of this

mechanism, but for convenience the main features are presented in an Appendix.

QLC-1 also has significant limitations. A structural limitation is that the time scale of the interconversion of quasi-liquid and ice relative to the other two processes (deposition/ablation and quasi-liquid/ice equilibration shown in Fig. 1) is fixed. In real crystal facets, these time scales could vary from facet to facet, or as a function of temperature and vapor pressure, and should therefore be adjustable quantities of the theory. A second shortcoming is that, as presented in N2016, inhomogeneities in the overlying vapor field used in simulations were limited to growth conditions, and of a form that relied on untested assumptions about the mathematical form of that inhomogeneity.

Our goal in the present communication is to generalize these insights from QLC-1 to a more diverse set of overlying vapor fields (including ablation conditions), and to narrow the number and range of parameters through the application of physical constraints and non-dimensionalization techniques. We also address the structural limitation in QLC-1 just mentioned, having to do with the time scale of quasi-liquid/ice equilibration dynamics. These are described in the next section.

2. Vapor Field (VF) theory. A key feature of the revised theory presented here is that the water vapor supersaturation profile is obtained from a simulation of the water vapor partial pressure, $P_{vap}(x, y)$, within a space surrounding an idealized, two-dimensional crystal. This is accomplished by integrating the two-dimensional diffusion equation

$$(2.1) \quad \frac{\partial P_{vap}}{\partial t} = D_{vap} \nabla^2 P_{vap}$$

where D_{vap} is the diffusion coefficient of water vapor through air, computed by

$$(2.2) \quad D_{vap} = D_{vap}^o \left(\frac{P_{total}}{1 \text{ atm}} \right) \left(\frac{T}{273 \text{ K}} \right)^{m_D}$$

where we have written P_{total} to indicate the combined pressure of water vapor and the ambient air (see [9]). Values of constants appearing in Eq. 2.2 are given in Table 1.

Eq. 2.1 is solved subject to Neumann and Dirichlet boundary conditions. The latter represents a constant, far-field vapor concentration, $\sigma_{I,\infty}$, at the outside boundary of a two-dimensional simulation space. Neumann conditions represent changes in water vapor at the crystal surface due to crystal growth or ablation,

$$(2.3) \quad -g_{ice} \times \rho_{ice} \times \frac{RT}{M_{H_2O}}$$

where g_{ice} is the growth rate of the ice surface, ρ_{ice} is the mass density of ice, and M_{H_2O} is the molar mass of water. The resulting supersaturation profiles adjacent to the ice surface of a given facet, defined relative to microsurface I of Fig. 1, are designated $\sigma_I(x)$ or $\sigma_I(y)$, depending on the spatial orientation of the facet (here, we will use only the former).

3. QLC-2 theory. The dynamics of ice crystal growth in the QLC-2 model are given by:

$$(3.1) \quad \frac{\partial N_{tot}}{\partial t} = D_{QLL} \nabla_x^2 N_{QLL} + \nu_{kin} \sigma_m(x, N_{QLL})$$

$$(3.2) \quad \frac{\partial N_{QLL}}{\partial t} = \frac{\partial N_{tot}}{\partial t} - \frac{N_{QLL} - N_{QLL}^{eq}(N_{tot})}{t_{eq}}$$

and have the following properties:

1. The operator $D_{QLL} \nabla_x^2$ in Eq. 3.1 represents surface diffusion of the QLL; it operates on N_{QLL} , rather than N_{tot} , to reflect the idea that the underlying ice is immobile on time scales considered here. The diffusion coefficient will be assumed here to depend on temperature according to

$$(3.3) \quad D_{QLL} = D_{QLL}^o \exp \left(-\frac{E_a}{R} \left(\frac{1}{T} - \frac{1}{T_0} \right) \right)$$

2. ν_{kin} is the rate at which vapor-phase water molecules strike the quasi-liquid. It is assumed that these stick with 100% efficiency, and thermalize on a picosecond time scale (i.e., instantaneously within the time scale of QLC-2 simulations). It can be obtained from the temperature according to the Hertz-Knudsen formula,

$$(3.4) \quad \nu_{kin} = P_{vap}^{eq}(T) \times \left(\frac{M_{H_2O}}{2\pi RT} \right)^{1/2}$$

where $P_{vap}^{eq}(T)$ is water's equilibrium vapor pressure, and M_{H_2O} is its molar mass.

3. The effective surface supersaturation, σ_m in Eq. 3.1, depends on the imposed surface supersaturation, $\sigma_I(x)$, obtained from VF simulations. We shall see that numerical results reveal patterns in the shape of $\sigma_m(x)$, and suggest analytical representations, as described in Section 4.
4. The form of the right-most term in Eq. 3.2, $\frac{N_{QLL} - N_{QLL}^{eq}(N_{tot})}{t_{eq}}$, is the primary departure of QLC-2 from QLC-1. The function $N_{QLL}^{eq}(N_{tot})$ appearing in the numerator prescribes the thickness of quasi-liquid when it is in equilibrium with the underlying ice,

$$(3.5) \quad N_{QLL}^{eq}(N_{tot}) = \bar{N} - N^* \sin(2\pi N_{tot}).$$

This formulation ensures that the QLL thickness varies continuously and periodically from the thin “surface I” (with thickness $\bar{N} - N^*$) to the thick “surface II” (with thickness $\bar{N} + N^*$). (Note the connection to work of (Benet et al., Eq. 8 [10]), that also shows a sinusoidal dependence.) The denominator t_{eq} is a first-order relaxation constant describing the time scale of quasi-liquid/ice equilibration shown at the left-hand side of Fig. 1.

Transformation of Eqs. 3.1 and 3.2 using constants $\tau = \frac{t}{t_{eq}}$ and $\chi = x/(D_{QLL} t_{eq})^{1/2}$ results in the nondimensional forms:

$$(3.6) \quad \frac{\partial N_{tot}}{\partial \tau} = \nabla_\chi^2 N_{QLL} + \omega_{kin} \sigma_m(\chi, N_{QLL})$$

$$(3.7) \quad \frac{\partial N_{QLL}}{\partial \tau} = \frac{\partial N_{tot}}{\partial \tau} - \left(N_{QLL} - N_{QLL}^{eq}(N_{tot}) \right)$$

where $\omega_{kin} = t_{eq}\nu_{kin}$. The utility of this transformation is that it exposes a key redundancy in the parameterization, namely, that since D_{QLL} and t_{eq} appear only as a product in the rescaled spatial coordinate χ , it is not necessary to explore dependence on those parameters independently.

4. Methods and parameterizations.

4.1. Integration methods. The vapor pressure equation of motion (Eq. 2.1) is integrated over time using Euler’s method. Parameters are given in the Appendix. The QLC-2 equations of motion are solved using a variety of methods ... ODE ... Runge-Kutta45 ...

4.2. Surface supersaturation parameterization. After designating a desired growth or ablation rate for the crystal surface g_{ice} , we seek a corresponding supersaturation profile $\sigma_I(x)$ that will result in that steady state growth rate. For a chosen growth rate, g_{ice} , a set of far-field supersaturation values ($\sigma_{I,\infty}$) is specified. A vapor field simulation for each candidate boundary condition $\sigma_{I,\infty}$ produces a corresponding $\sigma_I(x)$ profile, each of which is then provided as an input to a QLC-2 model run. The $\sigma_I(x)$ profile that yields a QLC-2 growth rate closest to g_{ice} is then used in subsequent QLC-2 simulations.

4.3. Other parameters.

1. $\bar{N} = 1$ and $N^* = 0.143$
2. $\sigma^o = 0.2$
3. $\Delta_N = 0.389$ nm (the thickness of a single layer of ice), to approximate the thickness of a prismatic facet bilayer
4. $L = 30$ μ m (the distance from facet center to corner)
5. $t_{eq} = 100$ ns (the ice-QLL equilibration time constant)
6. $T = 240$ K (temperature)
7. $g_{ice} = 1$ μ m/s (the growth / ablation rate of the crystal)

5. Results. Typical vaporfield results are shown in Fig. 2. Panels (a) and (b) of this figure demonstrate what we define here to be a “Bergian growth pattern”, namely, that the partial pressure of water vapor, P_{vap} , immediately above a growing faceted surface is greater at the extremes of the facet, i.e., at facet corners. Panels (c) and (d) show, however, an “anti-Bergian growth pattern”, namely, that when a bordering facet is growing quickly, the water vapor concentrations at facet corners are depleted by those bordering facets enough that the Bergian pattern is inverted, peaking in the center of the slow-growing facet. A third example, Panels (e) and (f), show what happens under subsaturated conditions with equal ablation rates across all four facets: namely, that water vapor concentration is highest at facet centers. We define that as a “Bergian ablation pattern”.

We also point out that profiles of P_{vap} such as those shown in the right-hand side Fig. 2 are well-approximated by a parabolic function of the distance coordinate x . This, in turn, means that the corresponding profiles of non-dimensional imposed surface supersaturation, defined by

$$(5.1) \quad \sigma_I(x) = \frac{P_{vap}(x) - P_{vap}^{eq}(T)}{P_{vap}^{eq}(T)}$$

(where $P_{vap}^{eq}(T)$ can be computed in the usual way, i.e., by the Clausius-Clapeyron equation corresponding to water vapor in equilibrium with ice) can also be approximated as a parabolic function of x . Therefore we write

$$(5.2) \quad \sigma_I(x) \approx \sigma_{I,\text{corner}} \times \left(c_r \left(\frac{x}{L} \right)^2 + (1 - c_r) \right)$$

where c_r (for “center reduction”) is the fractional reduction of supersaturation at facet centers relative to facet corners,

$$(5.3) \quad c_r = 1 - \frac{\sigma_{I,\text{middle}}}{\sigma_{I,\text{corner}}}$$

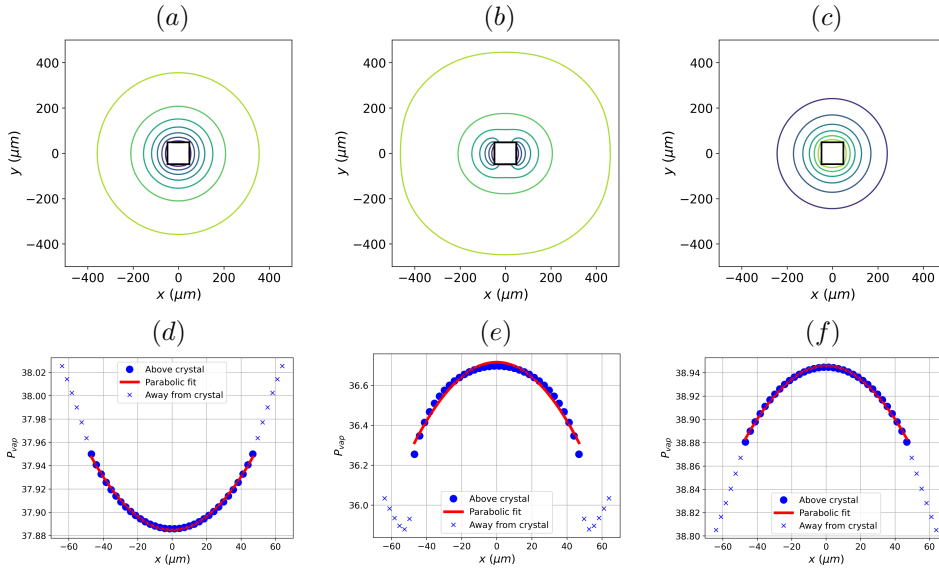


FIG. 2. (a) Steady-state water vapor partial pressures, $P_{vap}(x,y)$, around an ice crystal subjected to fixed (Dirichlet) supersaturated conditions in the far field. All four crystal surfaces, indicated by a black square at the center, are specified by Neumann conditions to be growing at the same rate. (b) P_{vap} along the upper facet of the crystal. High vapor pressures at the extreme left and right (i.e., at facet corners) define a “Bergian growth pattern”. (c) Like (a), but with asymmetric facet growth rates: the growth rates of the upper and lower facets are only a tenth of those at the left- and right-hand facets. (d) Like (b), but for the asymmetric facet growth rates shown in (c); high vapor pressures at facet centers define an “anti-Bergian growth pattern”. (e) Like (a), but under subsaturated conditions, with equal ablation rates at all four facet surfaces. (f) P_{vap} along the surface of the crystal. Low vapor pressures at facet corners under ablation conditions define a “Bergian ablation pattern”.

Under growth conditions, “Bergian growth pattern”, leads to $c_r > 0$, while under ablation conditions, the “Bergian ablation pattern” requires $c_r < 0$.

Implicit in the foregoing is an assumption about the microsurface of ice that one is referring to. In the present work, we have chosen microsurface I of Fig. 1 as that reference. Since at any given point on our modeled facet, the thickness of the QLL can range from that of microsurface I to microsurface II, we require a way to compute the effective surface supersaturation, σ_m , corresponding to other possible thicknesses of the QLL. Defining σ^o to be a measure of the difference in volatility of microsurface I and microsurface II, we adopt the formula

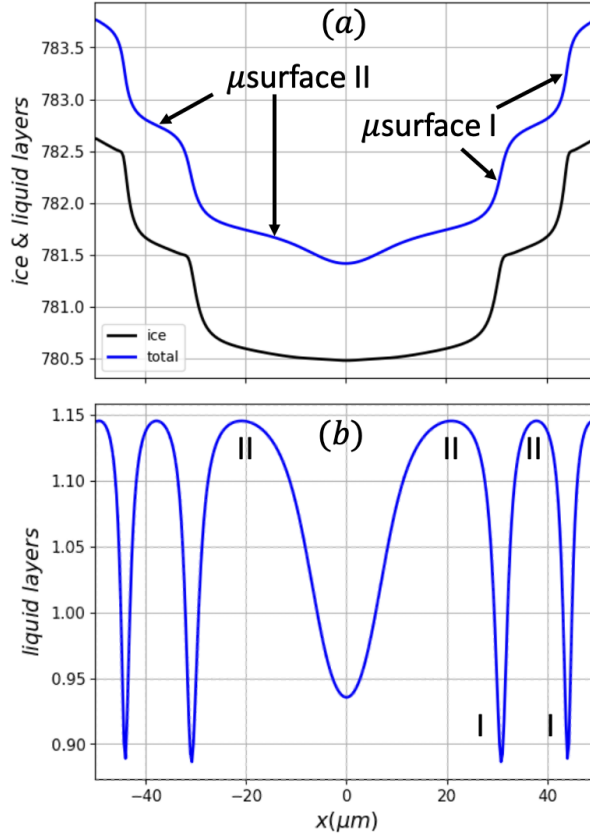


FIG. 3. An ice surface covered by QLL, as simulated by QLC-2.

$$(5.4) \quad \sigma_m(x) = \sigma_I(x) - \left(\frac{N_{QLL} - (\bar{N} - N^*)}{2N^*} \right) \sigma^o$$

In combination with Eq. 5.3, Eq. 5.4 ensures that microsurface I will have $\sigma_m(x) = \sigma_I(x)$, while microsurface II will have $\sigma_m(x) = \sigma_I(x) - \sigma^o$.

A typical trajectory result is shown in Fig. 3. Panel (a) shows that the surface is structured in steps, with broad, flat parts (“treads”), separated by abrupt increases in the surface height (“risers”). Panel (b) shows that the flat parts are close to the thick microsurface II, while the regions of abrupt increase are close to the thinner microsurface I. Dynamically, wherever a portion of the surface is microsurface I, since microsurface I is less volatile, that portion of the surface experiences a higher effective supersaturation (σ_m) than nearby portions of the surface that are the more volatile microsurface II.

Figure ?? shows a modeled ice crystal surface subjected to three overlying vapor field profiles. All lead to steady-state solutions, but the shape of those solutions depends on the shape of the vapor profile, as follows:

- Scenario “V-shaped supersaturated vapor field”: A “V”-shaped supersaturated water vapor profile is the profile expected for growing, isolated cirrus

ice crystals. After ≈ 100 ms, an initially-flat ice surface converges to a steady state profile in which the surface is convex-shaped, dominated by primarily microsurface I microstates, and growing at a constant rate. Faceted growth is facilitated by smaller λ at facet boundaries, which causes a localized reduction in the growth rate, compensating for the higher supersaturation at facet boundaries.

- Scenario “ Λ -shaped supersaturated vapor field”: A “ Λ ”-shaped supersaturated water vapor profile concentration profile is not expected for growing, isolated cirrus ice crystals, but it is plausible in SEM experiments when other crystals are nearby. After ≈ 100 ms, an initially-flat ice surface also converges, also to a steady state in which the surface is dominated by primarily microsurface I microstates, but in this case the overall shape is concave. Faceted growth is facilitated by smaller λ at facet center, which causes a reduction in the growth rate, compensating for the higher supersaturation at facet center.
- Scenario “ Λ -shaped subsaturated vapor field”: A “ Λ ”-shaped supersaturated water vapor profile concentration profile is expected for ablating isolated cirrus ice crystals. After ≈ 100 ms, an initially-flat ice surface converges to a steady state in which the surface is dominated by primarily microsurface II microstates, and is overall concave-shaped. Faceted ablation is facilitated by smaller λ at facet boundaries, which causes a reduction in the ablation rate, compensating for the more extreme subsaturation at facet boundaries.

Finally, we examine properties of these steady states. Because each crystalline lattice layer is a fixed thickness, the shape of a steady state profile such as those appearing in Fig. 5 can be summarized by the mean horizontal distance between successive molecular layers, defined as

$$(5.5) \quad \bar{\lambda}_{QLC2} = L/n_{steps}.$$

Conclusion... $\bar{\lambda}_{QLC2} \propto D^{1/2}$. Thus, we see that a key characteristic length predicted by QLC-2 depends on the square root of the surface diffusivity. This relationship between diffusion rate and characteristic length aligns with Turing’s analysis of pattern formation in reaction-diffusion systems. However, it should be borne in mind that the patterns of QLC-2 “steady states” are actually traveling-wave limit cycles, which are not considered in Turing’s analysis. Any such connection must overcome another hurdle as well, namely, that the depths of these characteristic distances are vastly different in QLC-2 compared to experiment: in the former it is a few monolayers, while in the latter it is thousands of monolayers.

In terms of facet resilience, we have seen that QLC-2 solutions and SEM-grown ice crystals both exhibit a propensity for perturbed states to recover when conditions favorable to faceting are restored, demonstrating the stability of these steady states.

6. Summary and Discussion. The QLC-2 model presented here offers significant technical improvements over the QLC-1 model reported in N2016, in that its equations of motion embody a more faithful representation of ice/QLL freeze/melt equilibration, as indicated by Molecular Dynamics simulations. That connection, in turn, enables the theory to represent a more unified picture of ice surface dynamics than has previously been possible. The model predicts facet convexity and concavity, a pattern that is echoed in reconstructions of SEM-grown ice crystals. The model also provides a mechanism by which real ice crystals resist dendritic geometries when subjected to supersaturation conditions (i.e., faceted growth), and how they also resist rounding when subjected to subsaturation conditions (faceted ablation). It is,

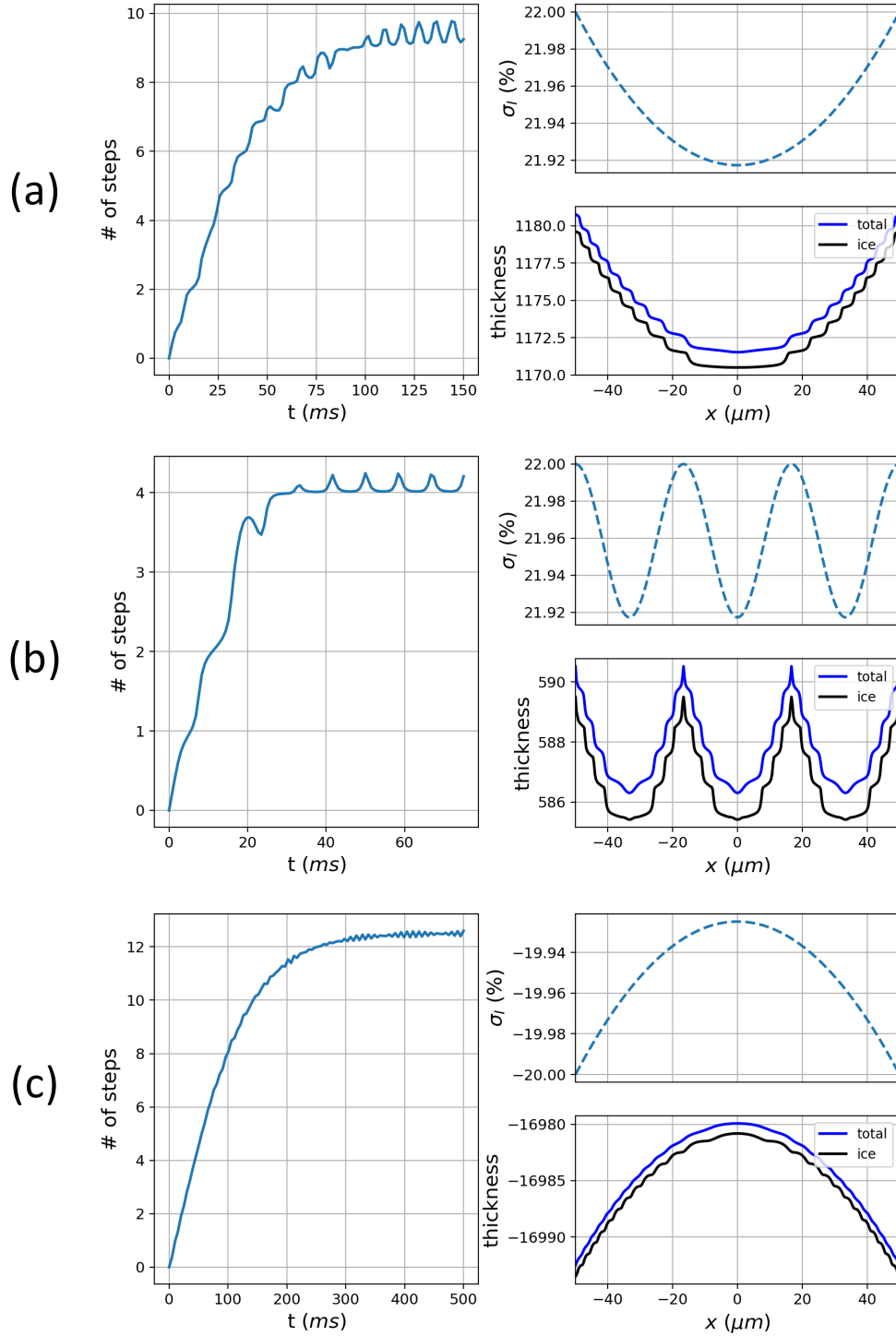


FIG. 4. Row (a): Dynamics of a surface subjected to parabolic supersaturation. The left-hand part of this row shows that the surface has converged to a limit cycle by 150 ns. In the upper right is shown the imposed supersaturation. The panel below that shows the limit cycle thickness (total ice, and ice only). Row (b): Dynamics when a corrugated supersaturation (sinusoidal) supersaturation pattern is imposed. Row (c): Dynamics when subsaturation conditions are imposed.

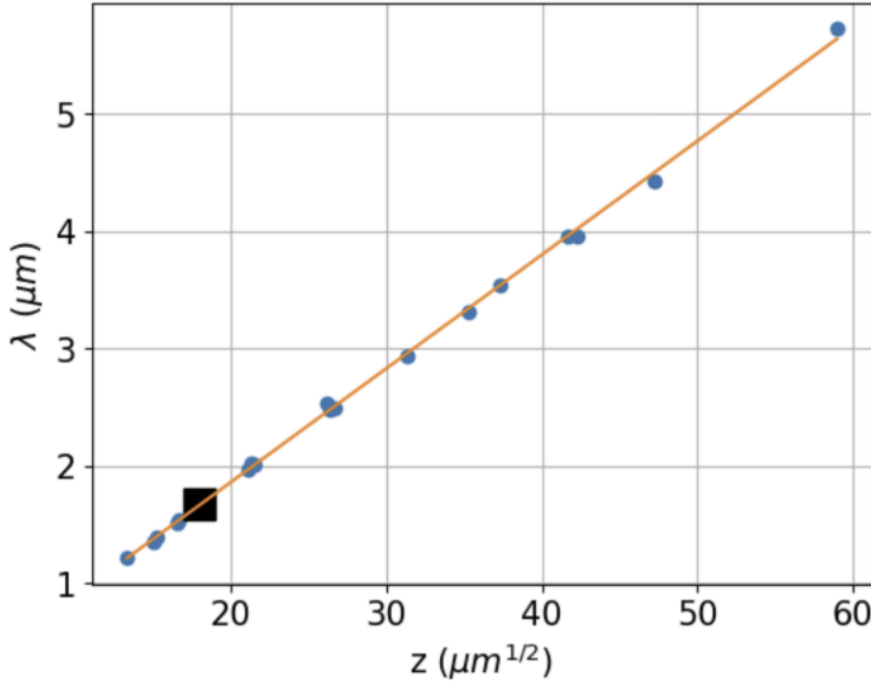


FIG. 5. Mean horizontal layer separation, $\bar{\lambda}$, as a function of $D_{QLL}...$

essentially, a theory of faceting that rests fundamentally on atomistic variations in the thickness and volatility of the quasi-liquid layer.

Qualitative implications of this work for cirrus cloud particles can be summarized as follows: As such particles fall through Earth's atmosphere, such crystals will encounter increased pressure, hence smaller D_{vap} , but also increased temperatures (unless there is an atmospheric inversion), hence larger D_{vap} . When the effect of increased pressure dominates, QLC-2 predicts enhanced growth at facet corners, hence greater facet convexity, and therefore a greater propensity toward hollowed crystal structures. When the effect of increased temperature dominates, however, we can expect more regular hexagonal shapes. Although there is no single observational datum that would help us resolve these predictions, we can comment that in exceptionally cold regions (such as the Antarctic Plateau), or even in mid-latitudes where high-altitude cryo-capture of ice crystals on ground-launched balloons is possible, observations have shown that cirrus clouds are frequently hollowed, suggesting dominance of increased pressure [11, 12, 13].

We should note that the results presented here do not consider variations in parameters σ^o , N^* , and \bar{N} , because these values are highly uncertain; more detailed molecular dynamics calculations could provide plausible values. In the meantime, we can speculate that because different facet types (basal, prismatic, or pyramidal) have distinct underlying crystal cell structures, their quasi-liquid properties will also be. Exploratory numerical studies varying the thickness of a single "layer" of ice has shown that a proportional increase in $\bar{\lambda}$ results. Preliminary numerical experiments varying N^* and \bar{N} have shown that...

A separate speculation concerns the observation that the $D^{1/2}$ dependence of

$\bar{\lambda}$ values exhibited by QLC-2 is the same as in Turing patterns. In one sense this should come as no surprise, since Turing’s theory, like QLC-2, is based on a reaction-diffusion equation. But there are also very big differences, including the fact that Turing’s analysis proceeds from an analysis of sensitivity to perturbations to an initially homogeneous distribution of chemical species, whereas the patterns in QLC-2 emerge as steady states of the equations of motion. The work of (Arioli and Koch 2015), on traveling-wave solutions of reaction-diffusion equations, is relevant here.

Finally, we note that the atoms-to-mesoscale approach represented in QLC-2 is not as fully integrated as we would like it to be ... maybe some insight from Jake’s heterogeneous multiscale approach is the way forward on this (Shohet et al. 2020).

Appendix A. QLC-1 Explanation of Faceted Growth. The main insight afforded by QLC-1 is that it provides a mechanism by which faceted ice crystal growth can occur, summarized as follows (the reader is referred to N2016 for a more complete and quantitative version of these arguments).

1. Designating the horizontal distance between new layers and their predecessors as “ λ ” (see 3), we see that $\lambda_{corner} < \lambda_{center}$; this is because new layers typically form at facet corners, where the water vapor concentration is highest, as described above.
2. Horizontal diffusion moves quasi-liquid away from microsurface II regions of the surface, toward microsurface I regions, because the former is thicker than the latter. The result is an overall increase in the average volatility of the surface, causing the surface as a whole to experience a net “diffusive slowdown” in its growth rate.
3. In regions where λ is small, QLL thickness gradients are large. In Fig. 3(b), for example, it is clear that the gradient in QLL thickness at I’ is greater than at I. It follows that, in a growing ice crystal, more diffusive slowdown occurs at facet corners.

In summary, a flat facet exposed to supersaturated vapor will initially experience higher growth rates at its corners, because of higher vapor concentration there, which leads to a higher step density (smaller λ) there, hence a reduction in the growth rate at corners relative to facet centers. When these effects become balanced – which can (and does) occur as an emergent property of the equations of motion defining QLC-1 (and QLC-2, as we will show here), the result is equal growth rates across the entire facet. The resulting traveling wave would be interpreted at the mesoscale (e.g., in a high-resolution optical or scanning electron microscopy experiments) as faceted growth.

Appendix B. Vapor field calculations.

TABLE 1
Parameters for simulation of the vapor field around a growing, square-shaped ice crystal.

Descriptor	Value
Simulation space dimensions	$X = Y = \pm 500 \text{ } \mu\text{m}$
Time step for integration	$dt = 5 \times 10^{-5} \text{ } \mu\text{s}$
Time interval for integration	$t_{max} = 2 \text{ } \mu\text{s}$
Spatial discretization	$dx = dy = 2.8 \text{ } \mu\text{m}$
Diffusion coefficient at $T = 273 \text{ K}$, $P_{total} = 1 \text{ atm}$	$D_{vap}^o = 21.9 \text{ } \mu\text{m}^2/\mu\text{s}$
Temperature	$T = 240 \text{ K}$
Total pressure	$P_{total} = 68.6 \text{ Pa}$
Diffusion Temperature-correction exponent	$m_D = 1.86$
Diffusion coefficient under ambient conditions	$D_{vap} = 3.49 \times 10^4 \text{ } \mu\text{m}^2/\mu\text{s}$
Far-field water vapor partial pressure	$P_{vap,f} = 30 \text{ Pa}$
Far-field water vapor supersaturation	$\sigma_I = 0.25$
Mass density of ice	$d_{ice} = 0.9 \text{ g/cm}^3$
Growth rate of ice surface	$g_{ice,s} = 2 \text{ } \mu\text{m/s}$

REFERENCES

- [1] Emma Järvinen, Bastiaan Van Dienenhoven, Nathan Magee, Steven Neshyba, Martin Schnaiter, Guanglang Xu, Olivier Jourdan, David Delene, Fritz Waitz, Simone Lolli, and others. Ice crystal complexity and link to the cirrus cloud radiative effect. pages 47–85. Publisher: Wiley Online Library.
- [2] Jerry Y Harrington and Gwenore F Pokrifka. Approximate models for lateral growth on ice crystal surfaces during vapor depositional growth. 78(3):967–981.
- [3] Pablo Llombart, Eva G Noya, and Luis G MacDowell. Surface phase transitions and crystal habits of ice in the atmosphere. 6(21):eaay9322. Publisher: American Association for the Advancement of Science.
- [4] T Kuroda and R Lacmann. Growth kinetics of ice from the vapour phase and its growth forms. 56(1):189–205. Publisher: Elsevier.
- [5] C Jayaprakash, WF Saam, and S Teitel. Roughening and facet formation in crystals. 50(25):2017. Publisher: APS.
- [6] Steven Neshyba, Erin Nugent, Martina Roeselová, and Pavel Jungwirth. Molecular dynamics study of ice- vapor interactions via the quasi-liquid layer. 113(11):4597–4604. Publisher: ACS Publications.
- [7] Ken-ichiro Murata, Ken Nagashima, and Gen Sazaki. How do ice crystals grow inside quasiliquid layers? 122(2):026102. Publisher: APS.
- [8] Steven Neshyba, Jonathan Adams, Kelsey Reed, Penny M Rowe, and Ivan Gladich. A quasi-liquid mediated continuum model of faceted ice dynamics. 121(23):14–035. Publisher: Wiley Online Library.
- [9] Air - diffusion coefficients of gases in excess of air.
- [10] Jorge Benet, Pablo Llombart, Eduardo Sanz, and Luis G MacDowell. Structure and fluctuations of the premelted liquid film of ice at the triple point. 117(20):2846–2864. Publisher: Taylor & Francis.
- [11] NB Magee, Andrew Miller, M Amaral, and A Cumiskey. Mesoscopic surface roughness of ice crystals pervasive across a wide range of ice crystal conditions. 14(22):12357–12371. Publisher: Copernicus GmbH.
- [12] Nathan Magee, Katie Boaggio, Samantha Staskiewicz, Aaron Lynn, Xuanyi Zhao, Nicholas Tusay, Terance Schuh, Manisha Bandamede, Lucas Bancroft, David Connolly, and others. Captured cirrus ice particles in high definition. 2020:1–27. Publisher: Göttingen, Germany.
- [13] Von P Walden, Stephen G Warren, and Elizabeth Tuttle. Atmospheric ice crystals over the antarctic plateau in winter. 42(10):1391–1405.